Chronic optogenetic activation of hippocampal pyramidal neurons replicates the proteome footprint of Alzheimer's disease-like pathology

Iason Keramidis[1,2], Martina Samiotaki[3], Romain Sansonetti[1], Johanna Alonso[1], Katerina Papanikolopoulou[4], Yves De Koninck[1,2]

Abstract

Neuronal overexcitability can disrupt synapse formation and strength and elicit synaptic changes which in turn give rise to neuronal hyperactivity, and eventually overall abnormal neural circuit processing. Such network disruption impairs neuronal function and survival, resulting in the onset of neurodegeneration and Alzheimer's disease. Yet, the sequence of synaptic changes that result from sustained neuronal hyperactivity remain elusive. To address this, we adopted an optogenetic stimulation strategy to generate a model of long-lasting neuronal hyperactivity in hippocampal pyramidal neurons. We applied this to both wild-type mice and in the 5xFAD mice presenting mutations that confer susceptibility to develop Alzheimer's disease in humans. We analyzed the proteome changes occurring after a month of daily chronic optogenetic stimulation, which surprisingly revealed shared proteomic signatures between photoactivated wild-type and 5xFAD mice. Proteins involved in translation, protein transport, autophagy, and more importantly in the Alzheimer's disease pathology were upregulated in wild-type mice. By contrast, optogenetic overdrive in the 5xFAD mice resulted in extensive downregulation of proteins participating in mRNA processing and phosphorylation. The footprint of protein change upon driving hyperactivity in the wild-type mice included downregulation of glutamatergic and GABAergic synapse proteins indicating potential disruption of synaptic transmission. Moreover, the target of rapamycin mTORC1 signaling pathway, involved in the onset of several neuropathological disorders, was hyperactive after the optogenetic activation in wild-type mice. In turn, these proteome and signalling changes in the hippocampus of wild-type mice resulted in spatial memory loss and notably augmented Aβ42 secretion. Altogether, these findings indicate that neuronal overexcitability and hyperactivity alone replicate the footprint of proteomic changes within the hippocampus seen in mice harboring Alzheimer's disease-linked mutations. Thus, sustained neuronal hyperactivity may contribute to synaptic transmission disruption, memory deficits and the neurodegenerative process associated with Alzheimer's disease.

1. CERVO Brain Research Centre, Quebec Mental Health Institute, Québec, QC, G1E 1T2, Canada.

2. Department of Psychiatry & Neuroscience, Université Laval, Québec, QC, G1V 0A6, Canada.

3. Institute for Bio-Innovation, Biomedical Sciences Research Center Alexander Fleming, 34 Fleming Street, 16672, Vari, Greece.

4. Institute for Fundamental Biomedical Research, Biomedical Sciences Research Center Alexander Fleming, 34 Fleming Street, 16672, Vari, Greece.

Correspondence to: Yves De Koninck

Introduction

Aberrant neuronal activity can impair synapse formation and strength resulting in disruption of synaptic plasticity. In turn, altered synaptic plasticity could reorganize synaptic connections ensuing runaway excitation or quiescence and eventually modify local neuronal circuits [1]. For neural circuits to maintain their characteristic firing patterns, neurons within the network undergo homeostatic changes at the cellular level, regulating synthesis and degradation of key synaptic proteins [2, 3]. Alterations perturbing these regulations have been linked with the onset of various brain disorders such as epilepsy and autism [4].

Neuronal hyperexcitability manifests early in Alzheimer's disease (AD) [5–7], leading to cortical and hippocampal hyperactivity [8, 9] and under certain conditions to epileptiform activity and seizures in rodents [10, 11] and humans [12]. Both amyloid-β (Aβ) and Tau have been found to induce neuronal hyperactivity through distinct cellular mechanisms [11, 13–16]. Concurrently, neuronal hyperactivity can increase Aβ secretion [17, 18] and promote pathological phosphorylation of Tau [19]. These observations suggest that Aβ and Tau can initiate a vicious cycle of neuronal hyperactivity in AD underlying neurodegeneration in disease. However, it still remains unknown whether neuronal hyperactivity alone can induce pathology mimicking neurodegeneration in AD.

Optogenetics has emerged as a powerful method to control the activity of genetically defined neurons allowing to study the function of selective brain circuits in physiological but also pathological conditions [20–22]. Stabilized step function opsins (SSFOs) allow also for long-lasting activation of neural circuits with just a brief light stimulation [23]. Such chronic optogenetic activation is necessary to model neurodegenerative disorders like AD for which neuronal activity is altered for long periods of time. We adopted a similar approach to generate a model of chronic neuronal hyperactivity in the hippocampus of wild-type (WT) and a transgenic mouse line carrying AD-linked mutations and demonstrated that evoked neuronal hyperactivity can disrupt synaptic signalling and facilitate an activity-driven neuropathology similar to AD.

Materials and Methods

Animals

Rodent experiments were carried out on male 5xFAD mice and their WT littermates bred and housed in the CERVO Brain Research Centre animal facility. The male 5xFAD and female B6SJLF1/J breeders were purchased from the Jackson Laboratory (#34840-JAX and #100012,

respectively). Mice were housed on a 12 h day/night cycle with *ad libitum* access to food and water. Mice were randomly assigned to experimental groups. All experiments were approved by the committee for animal protection of Universite Laval (CPAUL) and followed the guidelines from the Canadian Council for Animal Care.

Surgical Procedures and viral transduction

All viral constructs were produced by the CERVO Canadian Optogenetics and Vectorology Foundry Core Facility (RRID: SCR_016477). The tip of the optic fiber (200 µm core, 0.39 NA on 2.5 mm ceramic ferrules) was coated with 100 nL of a 1:1 mix of silk fibroin solution (Sigma 5154-20ML) and the viral vector AAV2/5-CaMKIIa-hChR2(C128S/D156A)-mCherry (henceforth referred to as AAV2/5-CaMKIIa-SSFO-mCherry; titer: 7.7 x 10^{12} GC/mL) or AAV2/8-CaMKIIa-tdTomato (titer: 1.3 x 10^{13} GC/mL), prior to the surgery, and left to dry for 15 hrs at 4 ºC as described in [24].

Stereotaxic surgeries were performed on mice (4-weeks old) maintained on isoflurane anaesthesia (1.5%-2% in O_2). Briefly, we removed the skin atop the cranium and a ~250-µm-diameter craniotomy was drilled over the hippocampus at coordinates relative to Bregma of: -2.30 mm rostro-caudal and -2.00 mm latero-medial. The optic fiber cannula was lowered 1.60 mm into the brain (-1.60 mm dorso-ventral) and fixed on the cranium with C&B Metabond® (Parkell Inc.). Following the surgery, mice were single-housed and the chronic optogenetic stimulation experiments started 4-5 weeks later.

For the optrode recordings, the same viral vectors were unilaterally infused into each side of the hippocampal CA1 (rostro-caudal: -2.30 mm, latero-medial: 2.00 mm, dorso-ventral: 1.60 mm). The infusion was performed with pulled borosilicate glass capillaries and a NANOLITER2020 injector (World Precision Instruments LLC). The *in vivo* optrode experiments started a minimum of 4 weeks later.

Optogenetic stimulation

After 4-5 weeks from the optic fiber implantation mice were optically stimulated for 2 s every 24 hrs (starting at 2-months of age) for 4 weeks with blue light (470 nm, 1 mW). The light was generated by an LED diode (ThorLabs M470F3) and delivered through fiber optics (200 µm core, 0.39 NA) to the implanted fiber optic cannulae.

61 ***In vivo* extracellular optrode recordings**

62 Simultaneous optical stimulation and electrical extracellular recording in the hippocampal CA1
63 was performed in WT male mice previously transduced with SSFO or tdTomato using a micro-
64 optrode [25, 26]. Briefly, mice were anesthetized with a mix of 100 mg ketamine, 15 mg xylazine
65 and 2.5 acepromazine per kg and placed in a stereotaxic frame on a temperature control pad. A
66 craniotomy was drilled over the hippocampus at coordinates relative to Bregma of: -2.30 mm
67 rostro-caudal and -2.00 mm latero-medial. A micro-optrode (6-8 µm tip diameter; 550 µm optical
68 core; 0.29 NA; 250 µm hollow core) was filled with 0.5 M potassium acetate solution, connected
69 to a 488 nm laser diode (Doric lenses) through a multimode optical fiber (200 µm optical core;
70 0.22 NA; ThorLabs) and lowered vertically to the brain. Electrophysiological recordings were
71 initiated at -1,3 mm ventral. A 2s long light pulse was delivered to activate the SSFO. The
72 extracellular electrophysiological signal was amplified (Neurodata IR183, Cygnus technology),
73 filtered (band pass, 300–3,000 Hz, model 440, Brownlee Precision), and digitized. The filtered
74 traces were analyzed with Spike2 (Cambridge Electronic Design). Events were detected and the
75 firing rate of individual neurons was plotted in peristimulus time histograms (PSTH) with 10 s bins.
76 Neurons for which the standard deviation of firing rate for the light pulse bin was 1.5 times superior
77 to the basal firing rate (average of the firing rate during the 60s preceding the pulse of light) were
78 considered activated.

79 **Sample Preparation**

80 For the proteomics analysis, brains were excised from anesthetized mice (30% urethane in saline)
81 within 30 min after optogenetic stimulation. The hippocampi were dissected, collected in sample
82 tubes, frozen immediately in liquid nitrogen and stored at -80 ℃ until use. 25 mg of frozen tissue
83 was lysed in 150 µL of freshly made lysis buffer (4% SDS, 0.1 M DTT, 100 mM Tris/HCl; pH 7.6)
84 and homogenized with an electric FisherBrand™ Pellet Pestle™ homogenizer (Thermo Fisher
85 Scientific). Homogenates were incubated at 95 ℃ for 3 min and centrifuged at 16,000 g for 5 min.
86 The supernatants were transferred into sample tubes and stored at -80 ℃.
87 For ELISA and immunoblots, tissue was harvested as before within 30 min after optogenetic
88 stimulation. 25 mg of frozen hippocampus tissue was homogenized in 150 µL of RIPA buffer (50
89 mM Tris-HCl, 150 mM NaCl, 1% Triton X-100, 0.5% Na deoxycholate, 0.1% SDS; pH 8.0).
90 Homogenates were incubated under constant agitation for 4 hrs at 4 ℃ for lysis. Lysates were
91 centrifuged at 17,200 g and 4 ℃ for 10 min. Supernatants were collected and stored at -30 ℃.

92 **Protein mass spectrometry**

93 Protein mass spectrometry analysis was performed in the Proteomics Facility of Biomedical
94 Sciences Research Centre Alexander Fleming. Four to five biological replicas for each condition
95 (WT + AAV2/8-CaMKIIa-tdTomato; WT + AAV2/5-CaMKIIa-SSFO-mCherry; 5xFAD + AAV2/8-
96 CaMKIIa-tdTomato; 5xFAD + AAV2/5-CaMKIIa-SSFO-mCherry) were analyzed. Briefly, proteins
97 of the lysed samples were processed according to the sensitive Sp3 protocol [27]. The reduced
98 cysteine residues were alkylated in 200 mM iodoacetamide (Acros Organics). 20 µg of beads (1:1
99 mixture of hydrophilic and hydrophobic SeraMag carboxylate-modified beads; GE Life Sciences)
100 were added to each sample in 50% ethanol. Protein clean-up was performed on a magnetic rack.
101 The beads were washed twice with 80% ethanol followed by one wash with 100% acetonitrile
102 (Fisher Chemical). The beads-captured proteins were digested overnight at 37 ℃ with 0.5 µg
103 trypsin/LysC mix in 25 mM ammonium bicarbonate under vigorous shaking (1200 rpm, Eppendorf
104 Thermomixer). The supernatants were collected and the peptides were purified by a modified Sp3
105 clean-up protocol and finally solubilized in the mobile phase A (0.1% formic acid in water), and
106 sonicated. Peptides concentration was determined through absorbance measurement at 280 nm
107 using a nanodrop instrument.
108 Peptides were analyzed by a liquid chromatography tandem mass spectrometry (LS-MS/MS) on
109 a setup consisting of a Dionex Ultimate 3000 nanoRSLC online with a Thermo Q Exactive HF-X
110 Orbitrap mass spectrometer. Peptidic samples were directly injected and separated on a 25 cm-
111 long analytical C18 column (PepSep, 1.9 μm^3 beads, 75 µm ID) using a 90 min long run. The full
112 MS was acquired in profile mode using a Q Exactive HF-X Hybrid Quadropole-Orbitrap mass
113 spectrometer operating in the scan range of 375-1400 m/z using 120 K resolving power with an
114 Automatic Gain Control (AGC) of 3×10^6 and a max IT of 60 ms followed by data independent
115 analysis (DIA) using 8 Th windows (39 loops counts) with 15 K resolving power with an AGC of 3
116 $\times 10^5$, a max IT of 22 ms and normalized collision energy (NCE) of 26.

117 **Label-free quantification and data analysis**

118 Orbitrap raw data were analyzed in DIA-NN 1.8 (Data-Independent Acquisition by Neural
119 Networks) against the complete Uniprot *Mus musculus* proteome (Downloaded April 16 2021)
120 supplemented with APP, presenilin, mCherry and ChR2. Search parameters were set to allow up
121 to two possible trypsin/P enzyme missed cleavages. A spectra library was generated from the
122 DIA runs and used to reanalyze them. Cysteine carbamidomethylation was set as a fixed
123 modification while N-terminal acetylation and methionine oxidations were set as variable

124 modifications. The match between runs (MBR) feature was used for all the analyses and the
125 output (precursor) was filtered at 0.01 false discovery rate (FDR). The protein inference was
126 performed on the gene level using only proteotypic peptides. The double pass mode of the neural
127 network classifier was also activated. Perseus (version 1.6.15.0) [28] was used for data
128 processing and statistical analysis. Proteins were subjected to filtering based on valid values
129 setting a threshold of 70% valid values in at least one group. Remaining missing values were
130 imputed separately for each column (based on the normal distribution using width of 0.3 and down
131 shift of 1.8). The statistically significant proteins were then Z-scored and visualized by Euclidean
132 hierarchical clustering as heat maps.
133 Gene-Ontology analysis was performed with GeneCodis [29] by uploading the list of altered
134 proteins based on the T-test two-sample comparisons. The interaction network analysis of
135 functional or physical protein to protein associations were performed with STRING (version 11.5)
136 [30].

137 **Immunoblots**

138 Hippocampal lysates were diluted in Laemmli buffer at a concentration of 10 µg per 20 µL and
139 denaturized for 5 min at 95 ℃. Proteins were separated in 4–15% Mini-PROTEAN® TGX Stain-
140 Free™ acrylamide gels (BioRad) and transferred onto 0.45 µm low-fluorescence PVDF
141 membranes (BioRad). Membranes were probed with the rabbit monoclonal anti-EAAT1 (Abcam
142 ab176557), anti-EAAT2 (Abcam ab205248), anti-S6 (Cell Signaling 2217), anti-S6 Ser240/244
143 (Cell Signaling 5364), anti-Rheb (Cell Signaling 13879), anti-c-Fos (Cell Signaling 2250) or the
144 rabbit polyclonal anti-Calbindin (Millipore ABN2192) in Tris-buffered saline containing 0.2%
145 Tween and 5% bovine serum albumin at 4 ℃. All antibodies were used at 1:1000, except from
146 the anti-S6 Ser240/244 which was used at 1:10000. The appropriate anti-mouse or anti-rabbit
147 IgG conjugated with IRDye©800 or IRDye©680, respectively, were used at 1:10000. Proteins
148 were visualized using a ChemiDoc Imaging System (BioRad) and the intensity of protein bands
149 was quantified using ImageJ (NIH). To normalize for sample loading, the intensity of total protein
150 (TLP) measured on the TGX Stain-Free™ gels was used as previously described [31].

151 **ELISA**

152 Levels of Aβ40 and Aβ42 in hippocampal samples were quantitated by Human/Rat β Amyloid
153 (40) ELISA kit (Wako 294-62501, LOT# WTL5240) and Human/Rat β Amyloid (42) ELISA kit
154 (Wako 290-62601, LOT# WTM4353) respectively. Both ELISAs were performed according to the

155 manufacturer recommendations, and the plates were read at 450 nm using a Eon microplate
156 reader (BioTek).

157 **Immunofluorescence**

158 A Leica Vibratome VT1220S (Leica Microsystems) was used to cut 100 µm coronal sections of
159 paraformaldehyde fixed brain tissue. Sections were rinsed 3 times in 0.1M phosphate-buffered
160 saline with 0.2% Triton X-100 (PBST) for 10 min, blocked for 1 hr with 10% Normal Goat Serum
161 (NGS) in PBST and then incubated for 15 hrs at 4 ℃ in primary anti-c-Fos (rabbit monoclonal,
162 1:2000, Cell Signaling 2250) diluted in PBST containing 4% NGS. Sections were washed in PBST
163 and subsequently incubated for 2 hrs at room temperature in AlexaFluor™ 488-conjugated goat
164 anti-rabbit (1:500, Invitrogen A11008) diluted in PBST containing 4% NGS. Tissue was mounted
165 on SuperFrost™ slides (Thermo Fisher Scientific 12-550-15) using a fluorescence mounting
166 medium with DAPI (Abcam ab104139) and cover-slipped.
167 All confocal images were acquired with a Zeiss LSM710 confocal laser scanning microscope.
168 Acquisitions were 12-bit images, 2048x2048 pixels with a pixel dwell time of 3.15 µs. A 40x Plan-
169 Apochromat oil objective (1.4 NA) was used for magnification. Tile scans were acquired at 12-
170 bits, 512x512 pixels (each tile) with a pixel dwell time of 0.64 µs and an x5 EC-Plan-Neofluar
171 objective (0.16 NA). Laser power, photomultiplier tube (PMT) settings, filters, dichroic mirrors,
172 scanning speed were kept constant for all acquisitions.

173 **Y-maze spatial memory test**

174 The Y-maze apparatus consisted of 3 identical arms (each 36.2 x 8.25 cm) in a Y configuration
175 (placed at 120° to each other) connected by a center polygonal area. The walls of the arms were
176 transparent so the animals could identify two distinct visual cues placed outside the apparatus to
177 facilitate spatial navigation. During the training phase, the mice were placed individually in the
178 maze and left freely to explore two arms, for 10 minutes, while the third arm was blocked by a
179 removable door. An hour later, the mice were returned to the maze and allowed to explore all
180 arms. The latency to enter the new (third) arm was measured for each mouse and used to score
181 the spatial memory performance of the mice. Between mice, the maze was cleaned with 70%
182 isopropyl solution to minimize scent cues. Entry into the arm was defined as a mouse placing all
183 four paws on the arm. For the mice receiving the daily optogenetic stimulation, the spatial memory
184 test was performed after the end of the 4 weeks-long stimulation protocol. The day of the test, the
185 mice receive a 2s light pulse before the beginning of the training phase.

186 **Statistical Analysis**

187 For the proteomic experiments, the statistical analysis of the label-free quantification intensities
188 was performed with Perseus (version 1.6.15) using a two sample t-test with a *P*-value less than
189 0.05 or an ANOVA for multiple sample tests with a *P*-value lower than of 0.05. For estimation
190 statistics based on effect size and confidence intervals [32], the data were uploaded and analyzed
191 on https://www.estimationstats.com/. The estimation plots show the mean difference between the
192 groups and the 95% confidence interval by the ends of the vertical error bar. Bar graphs were
193 generated with GraphPad Prism 9 (GraphPad software). Circos plots were drawn using RStudio
194 by uploading the list of proteins enriched in our samples for each biological process selected by
195 the gene-ontology analysis.

196 **Results**

197 **Optogenetic activation of the hippocampus in wild-type and 5xFAD mice using SSFO**

198 To generate a model of chronic neuronal hyperactivity in the rodent hippocampus we virally
199 transduced the SSFO-mCherry or tdTomato unilaterally under the CaM kinase II promoter
200 (CaMKIIa) into the CA1 of WT or 5xFAD [33] male mice (Fig. 1A, B). We then inserted an optic
201 fiber cannula above the CA1 and stimulated the infected neurons for 4 weeks by blue light (Fig.
202 1A). To validate whether light stimulation of the SSFO evoked neuronal activity, we performed
203 both immunostaining and immunoblot analysis for c-Fos on brain sections or in hippocampal
204 lysates, respectively. Coronal sections of mice infected with AAV-CaMKIIa-SSFO-mCherry in the
205 hippocampus showed mCherry labelling in the CA1, CA2 and CA3 (Fig. 1B). Thirty minutes after
206 light stimulation of mice expressing the SSFO-mCherry, the ipsilateral CA1, CA3 and dentate
207 gyrus (DG) neurons displayed increased c-Fos as compared to neurons of the contralateral side
208 (Fig. 1C). In mice infected with AAV-CaMKIIa-tdTomato, neurons in both hippocampus sides were
209 negative for c-Fos (Supplementary Fig. S1). The c-Fos expression levels were significantly higher
210 in hippocampal lysates from mice expressing SSFO as compared to tdTomato expressing mice
211 (Supplementary Fig. S2).
212 Using extracellular recordings in anesthetized mice we assessed the light-induced changes in the
213 activity of the CA1 region transduced either with the SSFO or tdTomato using a glass micro-
214 optrode we previously designed, which enables dual, co-registered electrophysiological recording
215 and optogenetic stimulation, free of photo-electric artefacts (Fig. 1D) [25, 26]. In mice expressing
216 the SSFO, the multiunit spike rates within the CA1 increased for several minutes after a 2s light

217 pulse as expected (Fig. 1E, F). Conversely, in tdTomato expressing mice, multiunit spiking activity
218 did not increase following the brief light pulse (Fig. 1E, F). Altogether, these results indicate that
219 the SSFO is transduced in the hippocampus and can be activated by light stimulation to generate
220 neuronal hyperactivity.

221 **Chronic optogenetic stimulation of the hippocampus activates protein translation and**
222 **phosphorylation but downregulates synaptic proteins in wild-type mice**

223 We sought to identify and quantify alterations in protein levels in response to sustain neuronal
224 hyperactivity in the hippocampus of mice. We analyzed the hippocampi of WT mice expressing
225 SSFO or tdTomato after 4 weeks of daily brief light stimulation (Fig. 1A) using label-free liquid
226 chromatography with tandem mass spectrometry (LC-MS/MS) proteomic analysis. We identified
227 778 proteins differentially abundant (P value ≤ 0.05) between the two conditions (Fig. 2A;
228 Supplementary Table S1). The chronic optogenetic stimulation in mice expressing SSFO
229 significantly upregulated the expression of 556 proteins and only downregulated the expression
230 of 222 proteins (Fig. 2A). Gene Ontology (GO) enrichment analysis with GeneCodis [29] revealed
231 that the abundant proteins were mainly part of the cytoplasmic and mitochondrial cellular
232 components (Fig. 2B). Yet, 77 of the proteins identified were part of the synapse (Fig. 2B) with
233 approximately 45% appearing downregulated, suggesting that synaptic function is altered by
234 evoked neuronal hyperactivity.
235 Moreover, GO analysis revealed that translation, protein transport, phosphorylation and
236 autophagy were among the most enriched biological processes found altered by the chronic
237 optogenetic stimulation (Fig. 2C). In turn, the AMPK signaling and ubiquitin-mediated proteolysis
238 were identified among the top 10 most enriched KEGG pathways (Fig. 2D). Surprisingly, the AD
239 pathway was also identified, with 31 proteins, all found upregulated in the WT+SSFO mice (Fig.
240 2D).
241 Out of the 34 downregulated synaptic proteins, interaction network analysis with STRING [30],
242 identified 19 proteins as glutamatergic synapse proteins, while 9 were enriched in GABAergic
243 synapses (Fig. 2E). And yet there are several more proteins, key for synaptic transmission, which
244 were found significantly downregulated in WT mice following chronic hippocampal hyperactivity
245 (Fig. 2E, F). Using immunoblots, we confirmed that Calbindin 1 (Calb1) was indeed
246 downregulated in hippocampal lysates from WT+SSFO expressing mice as compared to
247 WT+tdTom mice (Fig. 2G, H). Additionally, the excitatory amino acid transporter 1 (EAAT1 or
248 Slc1a3) was downregulated, while the excitatory amino acid transporter 2 (EAAT2 or Slc1a2) was

249 unaltered in the WT+SSFO mice (Figure 2G and 2H), consistent with the findings from the
250 proteomic analysis (Fig. 2A; Supplemental Table S1).

251 **Early AD pathology in 5xFAD mouse hippocampus largely mimics the footprint of altered**
252 **proteostasis caused by chronic optogenetic stimulation**

253 The 5xFAD mice exhibit amyloid deposition accompanied by cognitive deficits recapitulating
254 major features of Alzheimer's disease amyloid pathology [34]. Comparison of AD human and
255 rodent brain tissue revealed that the 5xFAD mice exhibit a proteomic signature similar to
256 symptomatic AD [35]. Moreover, an independent analysis of the mouse hippocampal proteome
257 focused on the proteomic changes during progression of the amyloid pathology [36]. In turn, we
258 analyzed the proteome changes manifesting in 3-month-old 5xFAD mice, to identify similarities
259 between the pre-symptomatic AD brain and the effect of hippocampal neuronal hyperactivity in
260 WT mice.
261 When we compared the proteins altered by the mutations and the AD pathology in the
262 hippocampus of 5xFAD mice, we identified 926 proteins as differentially expressed (Fig. 3A;
263 Supplementary Table S2). The majority of these proteins were upregulated (Fig. 3B). Protein
264 translation and transport, autophagy and phosphorylation were identified among the altered
265 biological processes in the 5xFAD mice (Fig. 3C), consistent with our findings in the WT+SSFO
266 mice (Fig. 2C). The mitochondria, synapse and endosomes were among the most enriched
267 cellular components (Fig. 3D). The majority of the abundantly expressed synaptic proteins belong
268 to the glutamatergic synapse, with 61% of them found downregulated in 5xFAD mice (Fig. 3D).
269 Interestingly, for biological processes such as translation, phosphorylation, autophagy and RNA
270 slicing the common proteins between the WT+SSFO and 5xFAD mice showed more than 50%
271 overlap between the two groups (Fig. 4A), as well as the same valence (Fig. 4B). For the proteins
272 found in the synapse the overlap was at 45.5% (Fig. 4A) and only Arr3 showed contrasting
273 valence between the two groups (Fig. 4B). Finally, the GO analysis identified 38 proteins
274 implicated in the AD pathway in the presymptomatic 5xFAD mice (Fig. 3B, E), with 19 of them
275 also found abundantly expressed in WT+SSFO mice (Fig. 4B, C, D), indicating that chronic
276 optogenetic activation of the hippocampus in WT mice induced signalling cascades involved in
277 the AD pathogenesis.

278 **Evoked chronic neuronal hyperactivity in the hippocampus of 5xFAD mice downregulates**
279 **mRNA splicing and protein phosphorylation**

280 We adopted the same approach to induce neuronal hyperactivity in the hippocampus of 5xFAD
281 mice (Fig. 1A). The chronic optogenetic stimulation in 5xFAD mice resulted in significantly
282 downregulating the expression levels of 264 proteins while it resulted in upregulating the levels of
283 only 99 proteins (Fig. 5A; Supplementary Table S3). The altered proteins were primarily
284 cytoplasmic, nucleic and part of the spliceosomal complex (Fig. 5B). Among the cellular
285 components greatly enriched, the glutamatergic synapse was identified with 29 proteins (Fig. 5B),
286 83% of which were downregulated. Three additional proteins of the GABAergic synapse were
287 found downregulated in the 5xFAD mice after the chronic optogenetic stimulation (Fig. 5C).
288 Contrary to the WT mice, GO enrichment analysis revealed that neurons in 5xFAD mice
289 responded distinctly to the induced neuronal hyperactivity by downregulating mRNA processing,
290 splicing and protein phosphorylation (Fig. 5D). Consistently, the spliceosome and RNA
291 degradation appeared among the most enriched KEGG pathways in the 5xFAD+SSFO mice (Fig.
292 5E). The purine and pyrimidine metabolism pathways were also affected (Fig. 5E). Lastly,
293 biological processes such as chemical synaptic transmission and synapse organization appeared
294 altered (Fig. 5F) by the chronic optogenetic stimulation in the 5xFAD mice. These findings indicate
295 that the 5xFAD mice respond distinctively to the chronic stimulation, as compared to the WT mice,
296 and thus the plasticity mechanisms induced by the stimulation in WT mice matches the changes
297 occurring at early rather than late stages of the AD pathogenesis.

298 **Degree of similarity in proteome changes caused by hyperactivity in WT brain *vs*. that in**
299 **AD-related pathology**

300 Hippocampal hyperactivity has been implicated in memory deterioration and AD pathogenesis [5,
301 12]. To further explore whether chronic optogenetic activation in the hippocampus of WT mice
302 indeed replicates some of the neurodegenerative processes involved in the pathogenesis of AD,
303 we performed a hierarchical clustering analysis based on our proteomic data. Accordingly, we
304 found that the WT+SSFO mice grouped together with the 5xFAD+tdTom while all the WT+tdTom
305 mice separated from the rest of mice according to the changes in protein levels (Fig. 6A).
306 Moreover, when we compared the proteins altered by stimulation in WT+SSFO mice to the ones
307 altered due to the mutations and AD-related pathology in the 5xFAD mice, we found that those
308 two groups resembles themselves much more than when comparing 5xFAD mice to unstimulated
309 control (only 135 protein changes in common; Fig. 6B).

310 The mammalian target of rapamycin complex 1 (mTORC1) is a principal signalling pathway
311 controlling protein translation initiation [37] and has been postulated to take part in AD pathology
312 [38]. Immunoblotting of hippocampal lysates revealed an increase in the phosphorylation of the
313 mTORC1 downstream translation initiation effector ribosomal protein S6 (rpS6; Fig. 6C, E),
314 concomitant with an increase in the expression of Rheb (Fig. 6C, D), the mTORC1 canonical
315 activator [39] in the WT+SSFO mice as compared to the WT+tdTom mice.
316

317 **Neuronal hyperactivity in wild-type mice induces spatial memory deficits and augments**
318 **Aβ42 secretion**

319 To further examine how chronic hippocampal hyperactivity and the synaptic transmission changes
320 (Fig. 2F) observed following the optogenetic stimulation impact brain function, we performed
321 behavioral testing of WT and 5xFAD mice. We adopted a modified version of the Y-maze
322 alternation test allowing for the evaluation of spatial memory performance in mice (Supplementary
323 Fig. S3). We found that chronic optogenetic stimulation in the hippocampus of WT+SSFO mice
324 resulted in spatial memory deficits, similar to the impairment seen here in 6-months-old 5xFAD
325 mice (Fig. 6F), or previously described in [40].
326 Finally, since previous observations have linked neuronal and network hyperactivity with an
327 increase in the secretion and deposition of amyloid-β in the brain of transgenic mice carrying
328 several AD-linked mutations [17, 18, 41, 42], we sought to measure the levels of soluble Aβ40
329 and Aβ42 in the brain of WT mice following our chronic optogenetic stimulation protocol. In the
330 hippocampus of WT+SSFO mice the levels of soluble secreted Aβ42 were significantly increased
331 as compared to the levels in the brain of WT+tdTom mice (Fig. 6H). The levels of Aβ40 showed
332 a trend of increase in the WT+SSFO mice, but this increase was not significantly different to the
333 Aβ40 levels in the WT+tdTom (Fig. 6H). Altogether, these results suggest that chronic neuronal
334 hyperactivity is sufficient to induce synaptic transmission disruption and memory loss similar to
335 that observed in the neurodegenerative process in AD, but also augments the amyloidogenic
336 cleavage of App.

337 Discussion

338 We adopted optogenetics and an SSFO to induce chronic neuronal hyperactivity and examine
339 the effect of such manipulation in the hippocampus of young WT and 5xFAD mice. We present
340 evidence of (1) an overt downregulation in the levels of both excitatory and inhibitory synaptic
341 proteins and an activation of translation, phosphorylation and autophagy following neuronal
342 hyperactivity in WT mice; (2) an upregulation of AD-associated proteins in WT+SSFO mice

343 mimicking the AD proteome signature found in the 5xFAD mice; (3) a downregulation in the levels
344 of proteins participating in RNA processing and protein phosphorylation in 5xFAD+SSFO mice;
345 (4) spatial memory impairments in WT+SSFO mice upon light stimulation; and (5) elevated levels
346 of soluble Aβ42 in WT hippocampi following chronic optogenetic stimulation. These findings
347 strongly support the notion that rampant neuronal hyperactivity distorts cellular mechanisms
348 regulating proteostasis similar to that seen in the prodromal phase of AD-like pathology. This
349 positions overt neuronal hyperactivity as a substrate of AD pathogenesis.
350 In various neurological disorders, cognitive decline has been associated with hippocampal
351 hyperactivity and the failure to deactivate brain regions consisting of the default mode network
352 (e.g. posterior cingulate cortex, precuneus, retrosplenial cortex) [5, 43–47]. Reducing neuronal
353 hyperactivity pharmacologically has been also found to improve cognitive performance in humans
354 with mild cognitive decline [48, 49] suggesting that neuronal hyperactivity is a cause and not a
355 compensatory mechanism of cognitive decline. But neuronal hyperactivity may have broader
356 implications in disease onset. Apart from contributing to cognitive deficits, neuronal hyperactivity
357 could drive several other pathological aspects related to AD, such as mTORC1 hyperactivity [50],
358 Aβ release [18], synaptic loss [51, 52] and neuronal degeneration [43].
359 It has been shown before that electrical, pharmacological and optogenetic neuronal stimulation
360 can augment the secretion of Aβ from the presynaptic terminals in various APP transgenic mouse
361 lines [17, 18, 41, 42]. In turn, elevated Aβ levels have been shown to induce neural overexcitability
362 and hyperactivity disrupting neural circuits both in WT and APP transgenic mouse lines [10, 13,
363 53]. Moreover, in humans, within the brain regions where Aβ aggregation is pronounced, the basal
364 metabolic rates and neuronal activity are profoundly elevated [8, 42, 54]. These findings support
365 the hypothesis of a vicious unclamped cycle facilitating an Aβ-dependent neuronal hyperactivity
366 in AD [13] and are in line with our results showing an increase in soluble Aβ42 secretion and a
367 multifactorial perturbation of synaptic transmission in WT animals following neuronal
368 hyperactivity.
369 The similarity we found in altered proteostasis and spatial memory in overstimulated WT and
370 5xFAD mice, together with the finding that neuronal hyperactivity in WT mice augments Aβ42
371 secretion establish chronic optogenetic stimulation in WT animals as a potential paradigm to
372 model sporadic AD-pathogenesis.
373 Finally, the distinct response to the chronic optogenetic stimulation in the 5xFAD, at least at the
374 proteome level, may reflect an occlusion of the detrimental effects of evoked neuronal
375 hyperactivity in AD, or a loss of proteostasis reserve. This is in line with observations indicating
376 that neuronal hyperactivity manifests early in AD resulting in synapse and circuit disruption [5, 6,

55, 56]. And yet, while these deficits in circuits arising from neuronal degeneration in AD might appear beyond repair, suppressing excessive neuronal activity early in the progression of the disease may represent a possible therapeutic modality to delay or modify the disease progression and cease the vicious cycle of relentless hyperactivity.

Data and code availability

The mass spectrometry proteomics data have been deposited to the ProteomeXchange Consortium *via* the PRIDE [57] partner repository with the dataset identifier PXD044437. The code used to generate the circos plot is available upon request. Any additional information required to reanalyze the data reported in this paper is available from the corresponding author upon request.

Acknowledgments

The authors thank Camille Sugère and Lyane Méthot for assistance with the daily optogenetic stimulation protocol and Drs Efthimios MC Skoulakis and Nicolò Ilacqua for their invaluable comments on the proteomics data. The authors also thank Dominique Isabel for assistance with RStudio and data visualization.

Funding

Weston Family Foundation Transformation Research grant TR192089 (YDK)
Canadian Institutes of Health Research (CIHR) grant FDN - 159906 (YDK)
Canada Research Chair program (YDK)
Norampac Research grant on Alzheimer's disease and Related Diseases (IK)
Fondation De La Famille Lemaire research grant on Alzheimer's disease and Related Diseases (IK)

Author Information

Iason Keramidis
Present address: CNC Program, Stanford University, Stanford, CA 94305, USA

Authors and affiliations

CERVO Brain Research Centre, Quebec Mental Health Institute, Québec, QC, G1E 1T2, Canada

Iason Keramidis, Romain Sansonetti, Johanna Alonso, Yves De Koninck
Department of Psychiatry & Neuroscience, Uuniversité Laval, Québec, QC, G1V 0A6, Canada
Iason Keramidis, Yves De Koninck
Institute for Bio-Innovation, Biomedical Sciences Research Center Alexander Fleming, 34 Fleming Street, 16672, Vari, Greece
Martina Samiotaki
Institute for Fundamental Biomedical Research, Biomedical Sciences Research Centre Alexander Fleming, 34 Fleming Street, 16672, Vari, Greece
Katerina Papanikolopoulou

Contribution

IK, KP and YDK designed the experiments. IK performed all the surgeries, the behavioral tests and ran the immunoblots and ELISAs. IK and RS performed the optogenetic stimulation and immunohistochemistry experiments. IK and JA conducted and analyzed the optrode experiments. MS performed the mass spectrometry analysis and the raw data processing. IK and KP analyzed the proteomics data. IK, KP and YDK interpreted the data and wrote the manuscript. YDK obtained funding and supervised all aspects of the present study. All the authors read and approved the final version of the manuscript.

Corresponding author

Correspondence to Yves De Koninck

Conflict of interest

The authors declare no competing interests.

References

1. Turrigiano GG, Nelson SB. Homeostatic plasticity in the developing nervous system. Nat Rev Neurosci 2004 52. 2004;5:97–107.

2. Wefelmeyer W, Puhl CJ, Burrone J. Homeostatic Plasticity of Subcellular Neuronal Structures: From Inputs to Outputs. Trends Neurosci. 2016;39:656–667.

3. Marder E, Goaillard JM. Variability, compensation and homeostasis in neuron and network function. Nat Rev Neurosci 2006 77. 2006;7:563–574.

4. Specchio N, Di Micco V, Trivisano M, Ferretti A, Curatolo P. The epilepsy-autism spectrum disorder phenotype in the era of molecular genetics and precision therapy. Epilepsia. 2022;63:6–21.

5. Palop JJ, Mucke L. Network abnormalities and interneuron dysfunction in Alzheimer disease. Nat Rev Neurosci. 2016;17:777–792.

6. Zott B, Busche MA, Sperling RA, Konnerth A. What Happens with the Circuit in Alzheimer's Disease in Mice and Humans? Annu Rev Neurosci. 2018;41:277–297.

7. Andersen J V., Skotte NH, Christensen SK, Polli FS, Shabani M, Markussen KH, et al. Hippocampal disruptions of synaptic and astrocyte metabolism are primary events of early amyloid pathology in the 5xFAD mouse model of Alzheimer's disease. Cell Death Dis 2021 1211. 2021;12:1–13.

8. Bassett SS, Yousem DM, Cristinzio C, Kusevic I, Yassa MA, Caffo BS, et al. Familial risk for Alzheimer's disease alters fMRI activation patterns. Brain. 2006;129:1229–1239.

9. Bookheimer SY, Strojwas MH, Cohen MS, Saunders AM, Pericak-Vance MA, Mazziotta JC, et al. Patterns of Brain Activation in People at Risk for Alzheimer's Disease. N Engl J Med. 2000;343:450–456.

10. Busche MA, Eichhoff G, Adelsberger H, Abramowski D, Wiederhold K-H, Haass C, et al. Clusters of hyperactive neurons near amyloid plaques in a mouse model of Alzheimer's disease. Science. 2008;321:1686–1689.

11. Verret L, Mann EO, Hang GB, Barth AMI, Cobos I, Ho K, et al. Inhibitory interneuron deficit links altered network activity and cognitive dysfunction in alzheimer model. Cell. 2012;149:708–721.

12. Vossel KA, Tartaglia MC, Nygaard HB, Zeman AZ, Miller BL. Epileptic activity in Alzheimer's disease: causes and clinical relevance. Lancet Neurol. 2017;16:311–322.

13. Zott B, Simon MM, Hong W, Unger F, Chen-Engerer HJ, Frosch MP, et al. A vicious cycle of β amyloid−dependent neuronal hyperactivation. Science (80-). 2019;365:559–565.

14. Ittner LM, Ke YD, Delerue F, Bi M, Gladbach A, van Eersel J, et al. Dendritic function of tau mediates amyloid-beta toxicity in Alzheimer's disease mouse models. Cell. 2010;142:387–397.

15. Roberson ED, Scearce-Levie K, Palop JJ, Yan F, Cheng IH, Wu T, et al. Reducing

464 endogenous tau ameliorates amyloid beta-induced deficits in an Alzheimer's disease
465 mouse model. Science. 2007;316:750–754.

466 16. Huijbers XW, Schultz AP, Papp K V., Lapoint MR, Hanseeuw X, Chhatwal XJP, et al. Tau
467 Accumulation in Clinically Normal Older Adults Is Associated with Hippocampal
468 Hyperactivity. J Neurosci. 2019;39:548–556.

469 17. Cirrito JR, Yamada KA, Finn MB, Sloviter RS, Bales KR, May PC, et al. Synaptic activity
470 regulates interstitial fluid amyloid-beta levels in vivo. Neuron. 2005;48:913–922.

471 18. Yamamoto K, Tanei Z-I ichi, Hashimoto T, Wakabayashi T, Okuno H, Naka Y, et al. Chronic
472 Optogenetic Activation Augments Aβ Pathology in a Mouse Model of Alzheimer Disease.
473 Cell Rep. 2015;11:859–865.

474 19. Frandemiche ML, De Seranno S, Rush T, Borel E, Elie A, Arnal I, et al. Activity-Dependent
475 Tau Protein Translocation to Excitatory Synapse Is Disrupted by Exposure to Amyloid-Beta
476 Oligomers. J Neurosci. 2014;34:6084–6097.

477 20. Kim CK, Adhikari A, Deisseroth K. Integration of optogenetics with complementary
478 methodologies in systems neuroscience. Nat Rev Neurosci 2017 184. 2017;18:222–235.

479 21. Ruthazer ES, Béïque JC, De Koninck Y. Editorial: Shedding Light on the Nervous System:
480 Progress in Neurophotonics Research. Front Neural Circuits. 2022;16:49.

481 22. Fenno L, Yizhar O, Deisseroth K. The Development and Application of Optogenetics.
482 Https://DoiOrg/101146/Annurev-Neuro-061010-113817. 2011;34:389–412.

483 23. Yizhar O, Fenno LE, Prigge M, Schneider F, Davidson TJ, O'Shea DJ, et al. Neocortical
484 excitation/inhibition balance in information processing and social dysfunction. Nature.
485 2011;477:171–178.

486 24. Jackman SL, Chen CH, Chettih SN, Neufeld SQ, Drew IR, Agba CK, et al. Silk Fibroin
487 Films Facilitate Single-Step Targeted Expression of Optogenetic Proteins. Cell Rep.
488 2018;22:3351–3361.

489 25. LeChasseur Y, Dufour S, Lavertu G, Bories C, Deschênes M, Vallée R, et al. A microprobe
490 for parallel optical and electrical recordings from single neurons in vivo. Nat Methods.
491 2011;8:319–325.

492 26. Dufour S, Koninck Y De. Optrodes for combined optogenetics and electrophysiology in live
493 animals. Https://DoiOrg/101117/1NPh23031205. 2015;2:031205.

494 27. Hughes CS, Moggridge S, Müller T, Sorensen PH, Morin GB, Krijgsveld J. Single-pot, solid-
495 phase-enhanced sample preparation for proteomics experiments. Nat Protoc 2018 141.
496 2018;14:68–85.

497 28. Tyanova S, Temu T, Sinitcyn P, Carlson A, Hein MY, Geiger T, et al. The Perseus
498 computational platform for comprehensive analysis of (prote)omics data. Nat Methods.
499 2016;13:731–740.

500 29. Garcia-Moreno A, López-Domínguez R, Villatoro-García JA, Ramirez-Mena A, Aparicio-
501 Puerta E, Hackenberg M, et al. Functional Enrichment Analysis of Regulatory Elements.
502 Biomedicines. 2022;10.

30. Szklarczyk D, Gable AL, Nastou KC, Lyon D, Kirsch R, Pyysalo S, et al. The STRING database in 2021: customizable protein-protein networks, and functional characterization of user-uploaded gene/measurement sets. Nucleic Acids Res. 2021;49:D605–D612.

31. Taylor SC, Berkelman T, Yadav G, Hammond M. A defined methodology for reliable quantification of western blot data. Mol Biotechnol. 2013;55:217–226.

32. Ho J, Tumkaya T, Aryal S, Choi H, Claridge-Chang A. Moving beyond P values: data analysis with estimation graphics. Nat Methods 2019 167. 2019;16:565–566.

33. Oakley H, Cole SL, Logan S, Maus E, Shao P, Craft J, et al. Intraneuronal β-Amyloid Aggregates, Neurodegeneration, and Neuron Loss in Transgenic Mice with Five Familial Alzheimer's Disease Mutations: Potential Factors in Amyloid Plaque Formation. J Neurosci. 2006;26:10129–10140.

34. Oblak AL, Lin PB, Kotredes KP, Pandey RS, Garceau D, Williams HM, et al. Comprehensive Evaluation of the 5XFAD Mouse Model for Preclinical Testing Applications: A MODEL-AD Study. Front Aging Neurosci. 2021;13:431.

35. Bai B, Wang X, Li Y, Chen PC, Yu K, Dey KK, et al. Deep Multilayer Brain Proteomics Identifies Molecular Networks in Alzheimer's Disease Progression. Neuron. 2020;105:975-991.e7.

36. Kim DK, Han D, Park J, Choi H, Park JC, Cha MY, et al. Deep proteome profiling of the hippocampus in the 5XFAD mouse model reveals biological process alterations and a novel biomarker of Alzheimer's disease. Exp Mol Med 2019 5111. 2019;51:1–17.

37. Hinnebusch AG, Ivanov IP, Sonenberg N. Translational control by 5′-untranslated regions of eukaryotic mRNAs. Science (80-). 2016;352:1413–1416.

38. Caccamo A, Majumder S, Richardson A, Strong R, Oddo S. Molecular interplay between mammalian target of rapamycin (mTOR), amyloid-β, and Tau: Effects on cognitive impairments. J Biol Chem. 2010;285:13107–13120.

39. Garami A, Zwartkruis FJT, Nobukuni T, Joaquin M, Roccio M, Stocker H, et al. Insulin activation of Rheb, a mediator of mTOR/S6K/4E-BP signaling, is inhibited by TSC1 and 2. Mol Cell. 2003;11:1457–1466.

40. Keramidis I, McAllister BB, Bourbonnais J, Wang F, Isabel D, Rezaei E, et al. Restoring neuronal chloride extrusion reverses cognitive decline linked to Alzheimer's disease mutations. Brain. 2023. 8 August 2023. https://doi.org/10.1093/BRAIN/AWAD250.

41. Kamenetz F, Tomita T, Hsieh H, Seabrook G, Borchelt D, Iwatsubo T, et al. APP Processing and Synaptic Function. Neuron. 2003;37:925–937.

42. Bero AW, Bauer AQ, Stewart FR, White BR, Cirrito JR, Raichle ME, et al. Bidirectional Relationship between Functional Connectivity and Amyloid-β Deposition in Mouse Brain. J Neurosci. 2012;32:4334–4340.

43. Putcha D, Brickhouse M, O'Keefe K, Sullivan C, Rentz D, Marshall G, et al. Hippocampal Hyperactivation Associated with Cortical Thinning in Alzheimer's Disease Signature Regions in Non-Demented Elderly Adults. J Neurosci. 2011;31:17680–17688.

542 44. Koh MT, Haberman RP, Foti S, McCown TJ, Gallagher M. Treatment strategies targeting
543 excess hippocampal activity benefit aged rats with cognitive impairment.
544 Neuropsychopharmacology. 2010;35:1016–1025.

545 45. Sperling RA, Laviolette PS, O'Keefe K, O'Brien J, Rentz DM, Pihlajamaki M, et al. Amyloid
546 deposition is associated with impaired default network function in older persons without
547 dementia. Neuron. 2009;63:178–188.

548 46. Oser N, Hubacher M, Specht K, Datta AN, Weber P, Penner IK. Default mode network
549 alterations during language task performance in children with benign epilepsy with
550 centrotemporal spikes (BECTS). Epilepsy Behav. 2014;33:12–17.

551 47. Seidman LJ, Rosso IM, Thermenos HW, Makris N, Juelich R, Gabrieli JDE, et al. Medial
552 temporal lobe default mode functioning and hippocampal structure as vulnerability
553 indicators for schizophrenia: A MRI study of non-psychotic adolescent first-degree
554 relatives. Schizophr Res. 2014;159:426–434.

555 48. Miller SL, Celone K, DePeau K, Diamond E, Dickerson BC, Rentz D, et al. Age-related
556 memory impairment associated with loss of parietal deactivation but preserved
557 hippocampal activation. Proc Natl Acad Sci U S A. 2008;105:2181–2186.

558 49. Bakker A, Krauss GL, Albert MS, Speck CL, Jones LR, Stark CE, et al. Reduction of
559 Hippocampal Hyperactivity Improves Cognition in Amnestic Mild Cognitive Impairment.
560 Neuron. 2012;74:467–474.

561 50. Henry FE, Wang X, Serrano D, Perez AS, Carruthers CJL, Stuenkel EL, et al. A Unique
562 Homeostatic Signaling Pathway Links Synaptic Inactivity to Postsynaptic mTORC1. J
563 Neurosci. 2018;38:2207–2225.

564 51. Lacor PN, Buniel MC, Furlow PW, Clemente AS, Velasco PT, Wood M, et al. Aβ Oligomer-
565 Induced Aberrations in Synapse Composition, Shape, and Density Provide a Molecular
566 Basis for Loss of Connectivity in Alzheimer's Disease. J Neurosci. 2007;27:796–807.

567 52. Hefendehl JK, LeDue J, Ko RWY, Mahler J, Murphy TH, MacVicar BA. Mapping synaptic
568 glutamate transporter dysfunction in vivo to regions surrounding Aβ plaques by iGluSnFR
569 two-photon imaging. Nat Commun 2016 71. 2016;7:1–13.

570 53. Busche MA, Kekuš M, Adelsberger H, Noda T, Förstl H, Nelken I, et al. Rescue of long-
571 range circuit dysfunction in Alzheimer's disease models. Nat Neurosci. 2015;18:1623–
572 1630.

573 54. Buckner RL, Snyder AZ, Shannon BJ, LaRossa G, Sachs R, Fotenos AF, et al. Molecular,
574 Structural, and Functional Characterization of Alzheimer's Disease: Evidence for a
575 Relationship between Default Activity, Amyloid, and Memory. J Neurosci. 2005;25:7709–
576 7717.

577 55. Styr B, Slutsky I. Imbalance between firing homeostasis and synaptic plasticity drives early-
578 phase Alzheimer's disease. Nat Neurosci. 2018;21:463–473.

579 56. Selkoe DJ. Alzheimer's Disease: Genes, Proteins, and Therapy. Physiol Rev.
580 2001;81:741–766.

581 57. Perez-Riverol Y, Bai J, Bandla C, García-Seisdedos D, Hewapathirana S, Kamatchinathan
582 S, et al. The PRIDE database resources in 2022: a hub for mass spectrometry-based
583 proteomics evidences. Nucleic Acids Res. 2022;50:D543–D552.

584

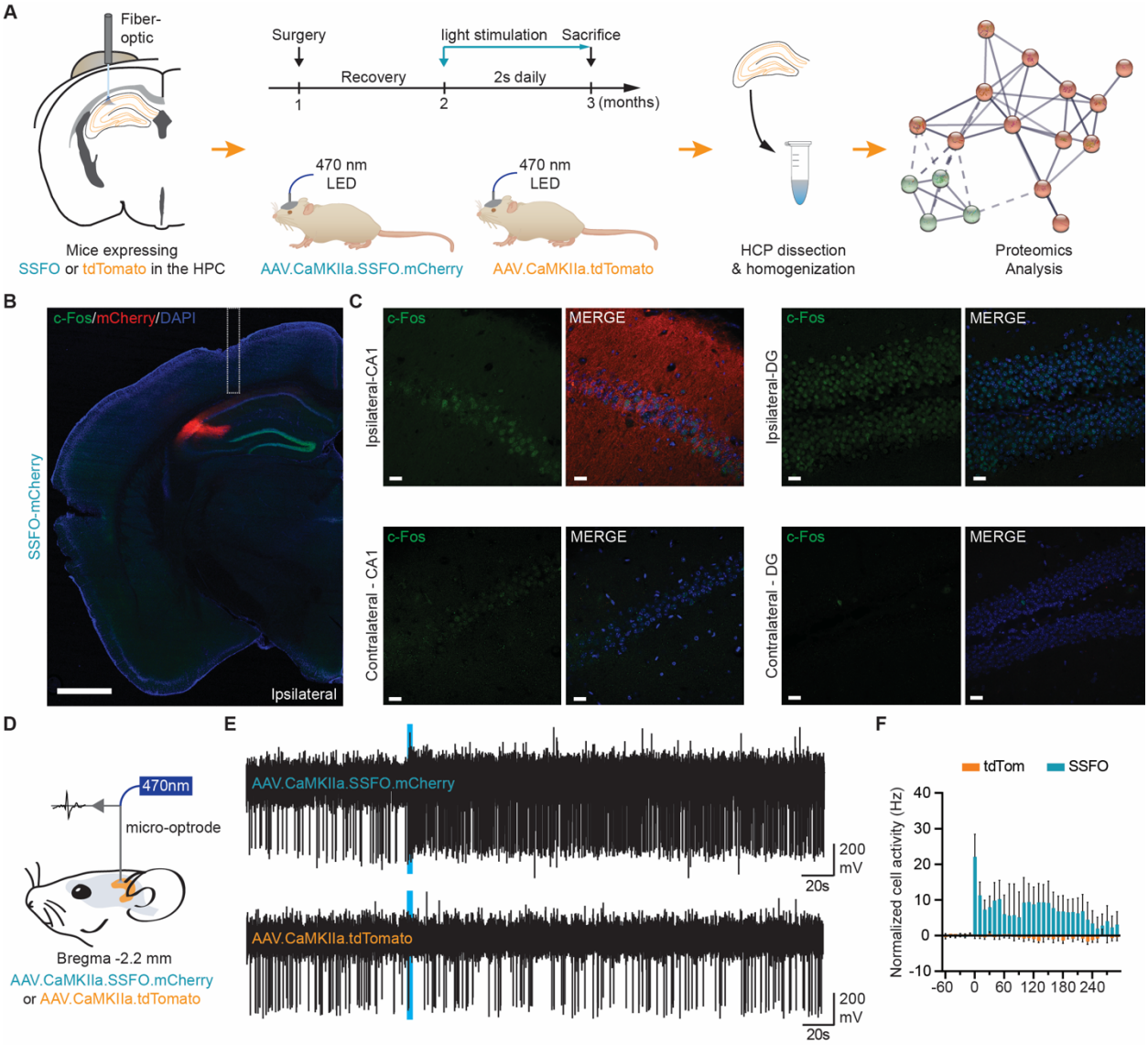

Fig. 1: SSFO optogenetic stimulation activates hippocampal neurons and evokes neuronal hyperactivity. (**A**) Diagram showing an overview of the proteome experiment following chronic optogenetic stimulation of the hippocampus (HPC). (**B** - **C**) Confocal images showing immunofluorescence labeling of c-Fos (green) and mCherry (virus expression reporter protein, red) in coronal sections of mice infected with AAV-SSFO (Scale bars: 1 mm in **B** and 20 μm in **C**; DAPI in blue). Expression of SSFO was observed in the ipsilateral side of infection, but not the contralateral side. Unilateral light stimulation increased the levels of c-Fos at ipsilateral CA1 and DG but not the contralateral side. (**D**) Micro-optrode recording configuration. A 470 nm laser was coupled to an optrode probe for electrical recordings and advanced into the brain. (**E**) Example traces recorded in AAV-SSFO (top) or AAV-tdTomato (bottom) infected mice. 470 nm activation pulse is indicated with a blue bar. (**F**) Peristimulus time histogram of the mean cell activity of

neurons recorded from mice infected with AAV-SSFO (n = 10; cyan) or AAV-tdTomato (n = 6; orange). Data presented as mean ± SEM.

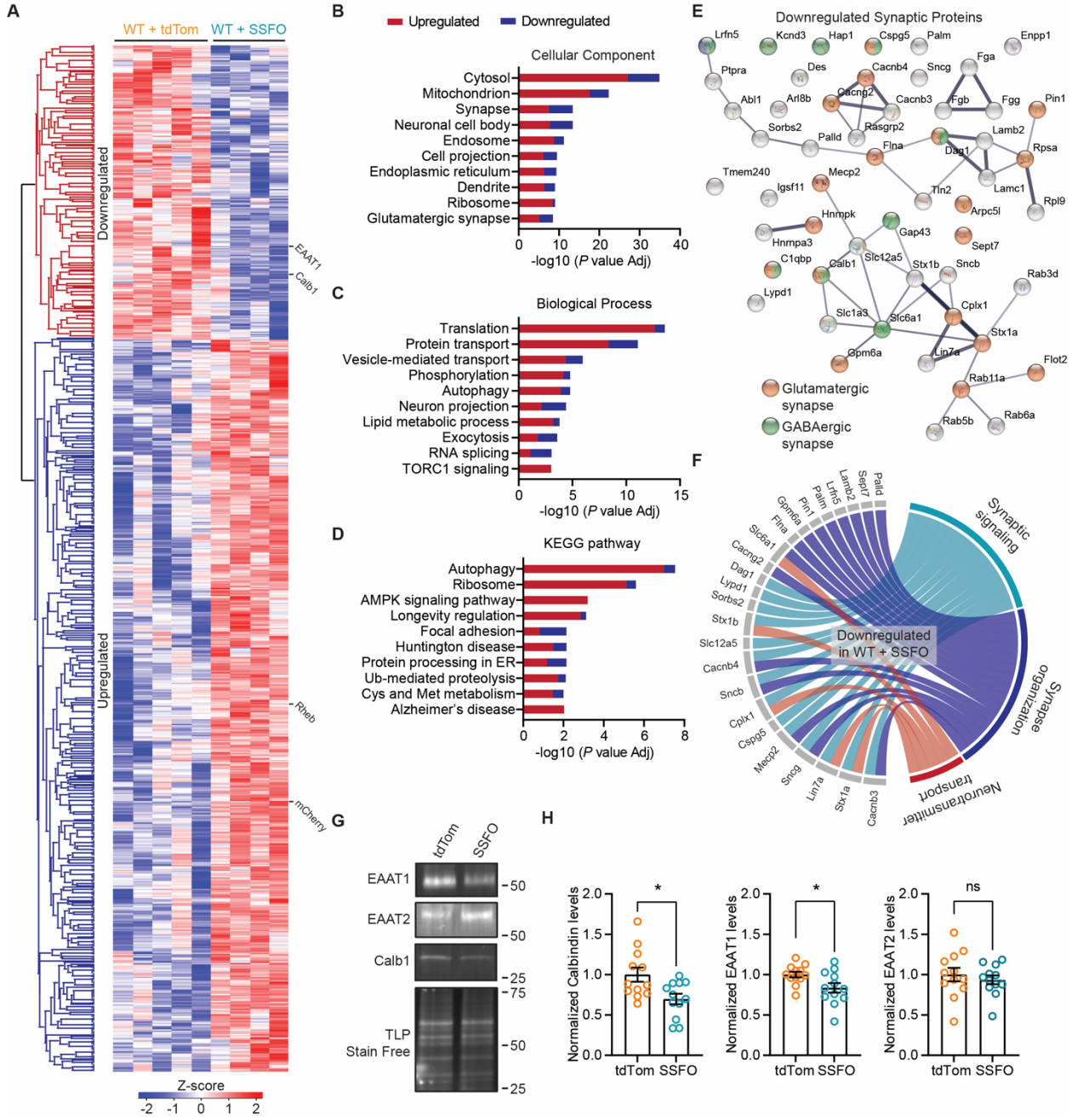

Fig. 2: Chronic optogenetic stimulation elicits synaptic signalling protein downregulation in wild-type mice. (**A**) Heat map illustrating the clustering of proteins (*P* value ≤ 0.05) in the hippocampus of WT mice expressing SSFO or tdTomato after 4 weeks of daily optogenetic stimulation. The color-coded scale (Z-score) denotes the upregulated (red) and downregulated (blue) proteins. (**B** - **D**) Results of the GO enrichment analysis of the top 10 most abundant cellular components (**B**), biological processes (**C**) and KEGG pathways (**D**) in the hippocampus of WT+SSFO mice. In red or blue the fraction of the total proteins upregulated or downregulated, respectively, for each GO-term. (**E**) Interactome of functional or physical protein to protein

608 associations of the synaptic proteins found downregulated in WT+SSFO mice. The proteins in
609 orange are associated with glutamatergic synapses while the proteins in green with GABAergic.
610 (**F**) Circos plots showing the proteins and selected biological processes downregulated in
611 WT+SSFO mice. (**G**) Representative immunoblots for the levels of Calbindin (Calb1), EAAT1 and
612 EAAT2 in hippocampal lysates from WT+SSFO and WT+tdTom mice. (**H**) Quantification of
613 Calbindin, EAAT1 and EAAT2 protein levels measured by immunoblotting in WT+SSFO (cyan; *n*
614 = 12) and WT+tdTom (orange; *n* = 12) mice after chronic optogenetic stimulation. The total protein
615 (TLP) levels measured on TGX Stain-Free gels is the loading control.

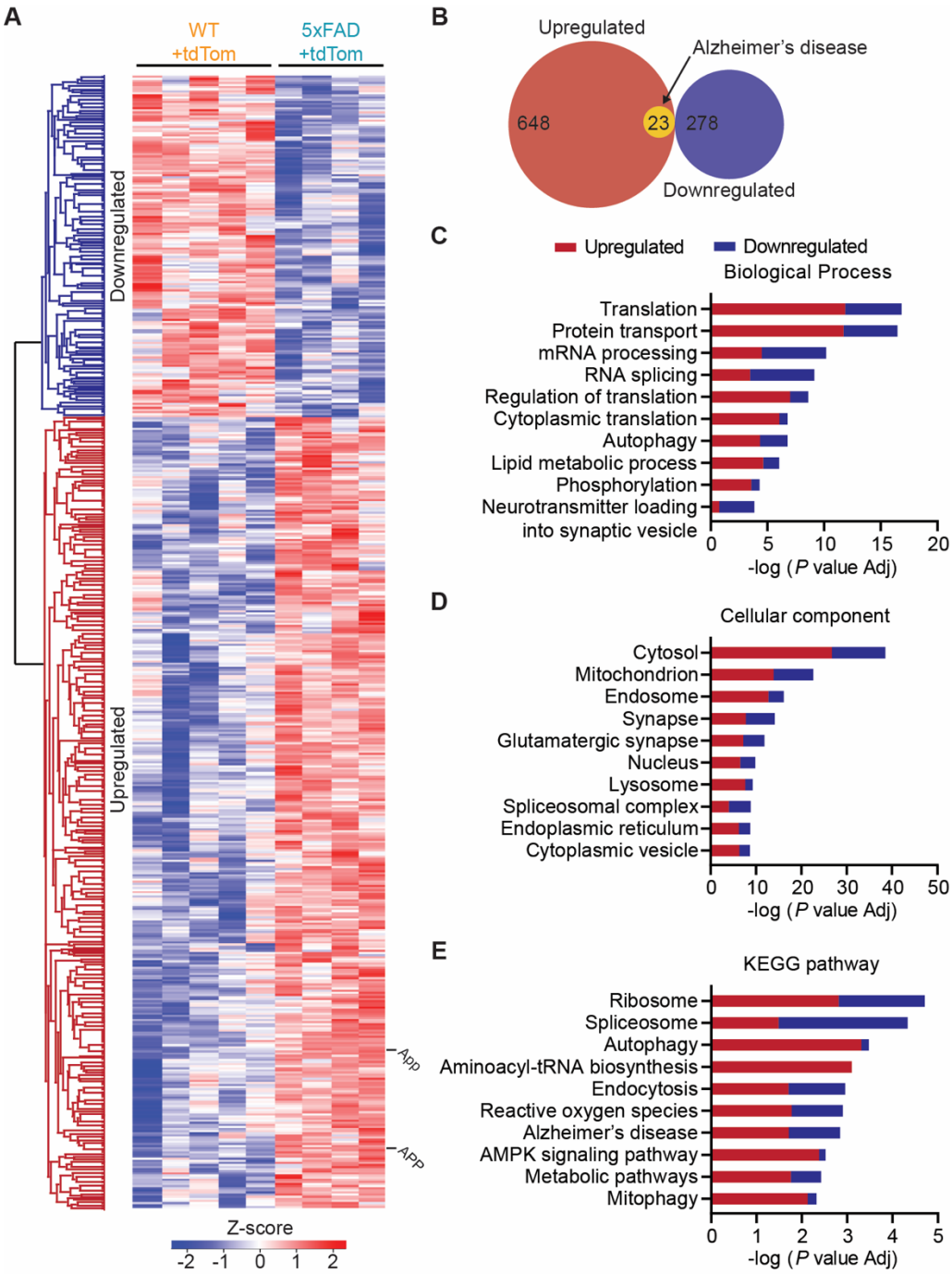

Fig. 3: Early AD pathology alters translation, phosphorylation and autophagy in the hippocampus of 5xFAD mice. (**A**) Heat map illustrating the scaled protein levels in the hippocampus of 3-month-old 5xFAD mice. The color-coded scale (Z-score) denotes the upregulated (red) and downregulated (blue) proteins. (**B**) Venn diagram showing the number of upregulated (red) and downregulated (blue) proteins in 5xFAD mice. In yellow the number of upregulated proteins found enriched in the AD KEGG pathway. (**C - E**) The results of the GO enrichment analysis of the top 10 most abundant biological processes (**C**), cellular components

624 (**D**) and KEGG pathways (**E**) in the hippocampus of 5xFAD mice. The colors in each bar represent
625 the fraction of the total proteins for each GO-term found upregulated (red) or downregulated
626 (blue).

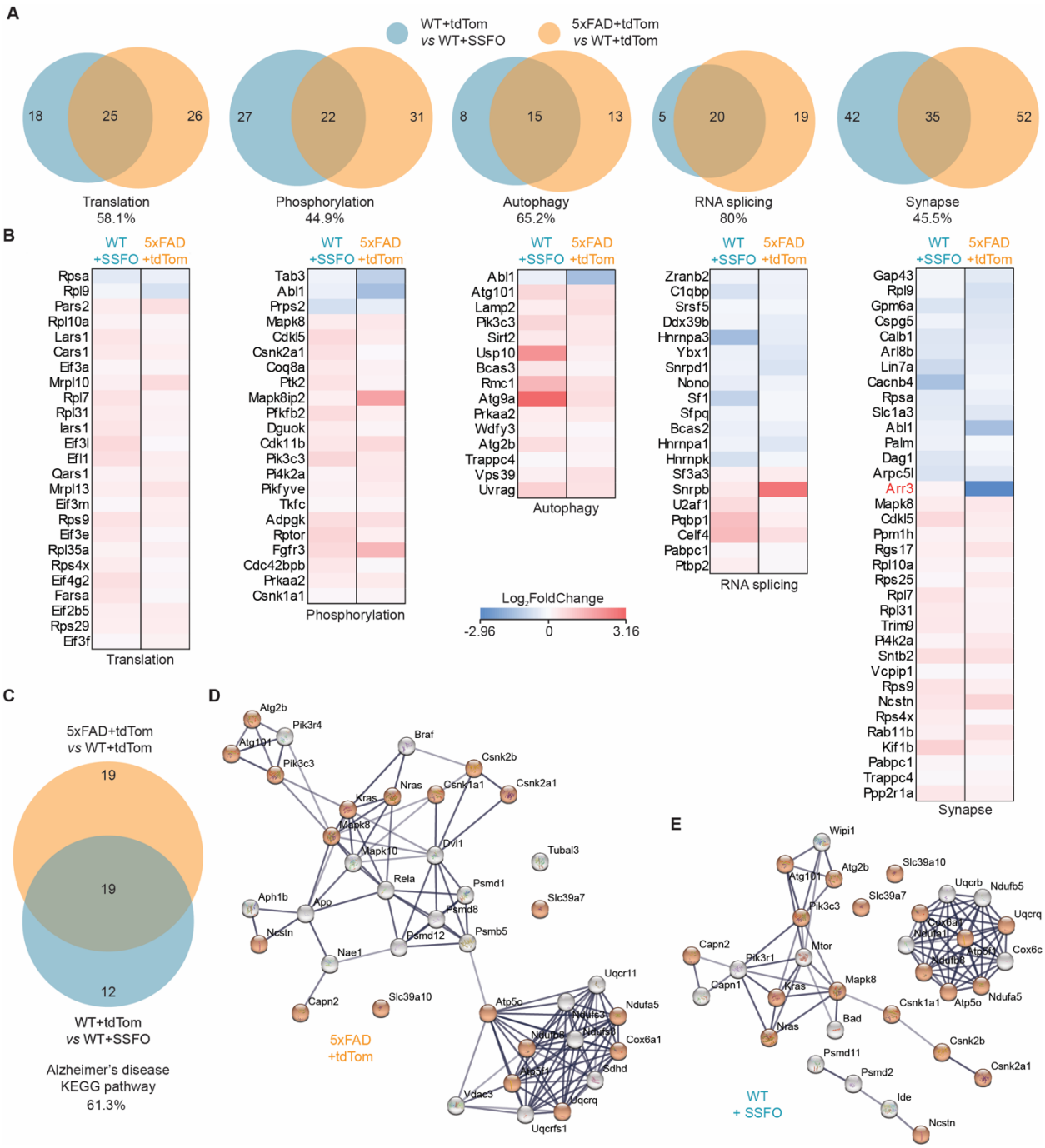

Fig. 4: Chronic optogenetic activation of the hippocampus in wild-type mice induces proteome changes involved in the early AD pathogenesis. (**A**) Venn diagrams illustrating the number of the abundant proteins for each GO-term found in the hippocampus of WT+SSFO and 5xFAD+tdTom mice. The percentages represent the fraction of the WT+SSFO altered proteins commonly found altered in the 5xFAD mice. (**B**) Heat maps revealing the fold of change in levels for the common proteins of each GO-term in **A** in the WT+SSFO or 5xFAD+tdTom mice. (**C**) The number of common proteins participating in the AD KEGG pathway when comparing the altered

635 proteins in the 5xFAD mice and the proteins altered in the WT+SSFO after the chronic optogenetic
636 stimulation. (**D - E**) Interactomes of functional or physical protein to protein associations of the AD
637 KEGG pathway proteins found altered in 5xFAD+tdTom (**D**) and WT+SSFO (**E**) mice.

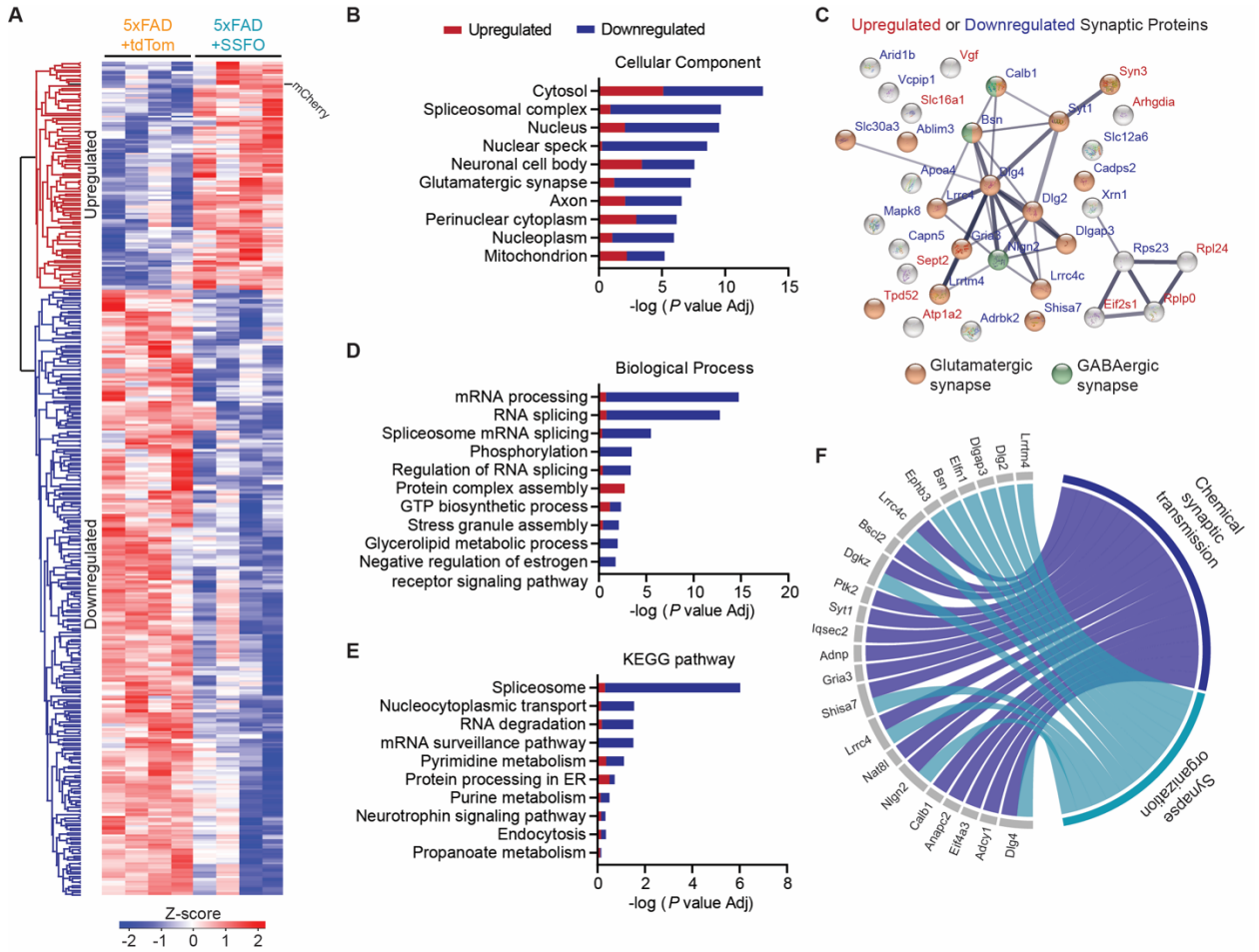

Fig. 5: Chronic optogenetic stimulation downregulates RNA processing and protein phosphorylation in 5xFAD mice. (**A**) Heat map revealing the scaled protein levels in the hippocampus of 5xFAD mice expressing SSFO or tdTomato after 4 weeks of daily optogenetic stimulation. (**B**) GO enrichment analysis showing the top 10 most abundant biological processes. In red or blue the fraction of the total proteins upregulated or downregulated for each GO-term, respectively (**C**) Interactome of functional or physical protein to protein associations of the synaptic proteins altered in 5xFAD+SSFO mice after optogenetic stimulation. The orange circles represent glutamatergic synapse proteins while the green GABAergic. The proteins written in red are upregulated while the proteins in blue are downregulated. (**D** - **E**) Same as in **B** but for the top 10 cellular components (**D**) and KEGG pathways (**E**) in the hippocampus of 5xFAD+SSFO mice. (**F**) Circos plots showing selected biological processes and the proteins altered in 5xFAD+SSFO mice.

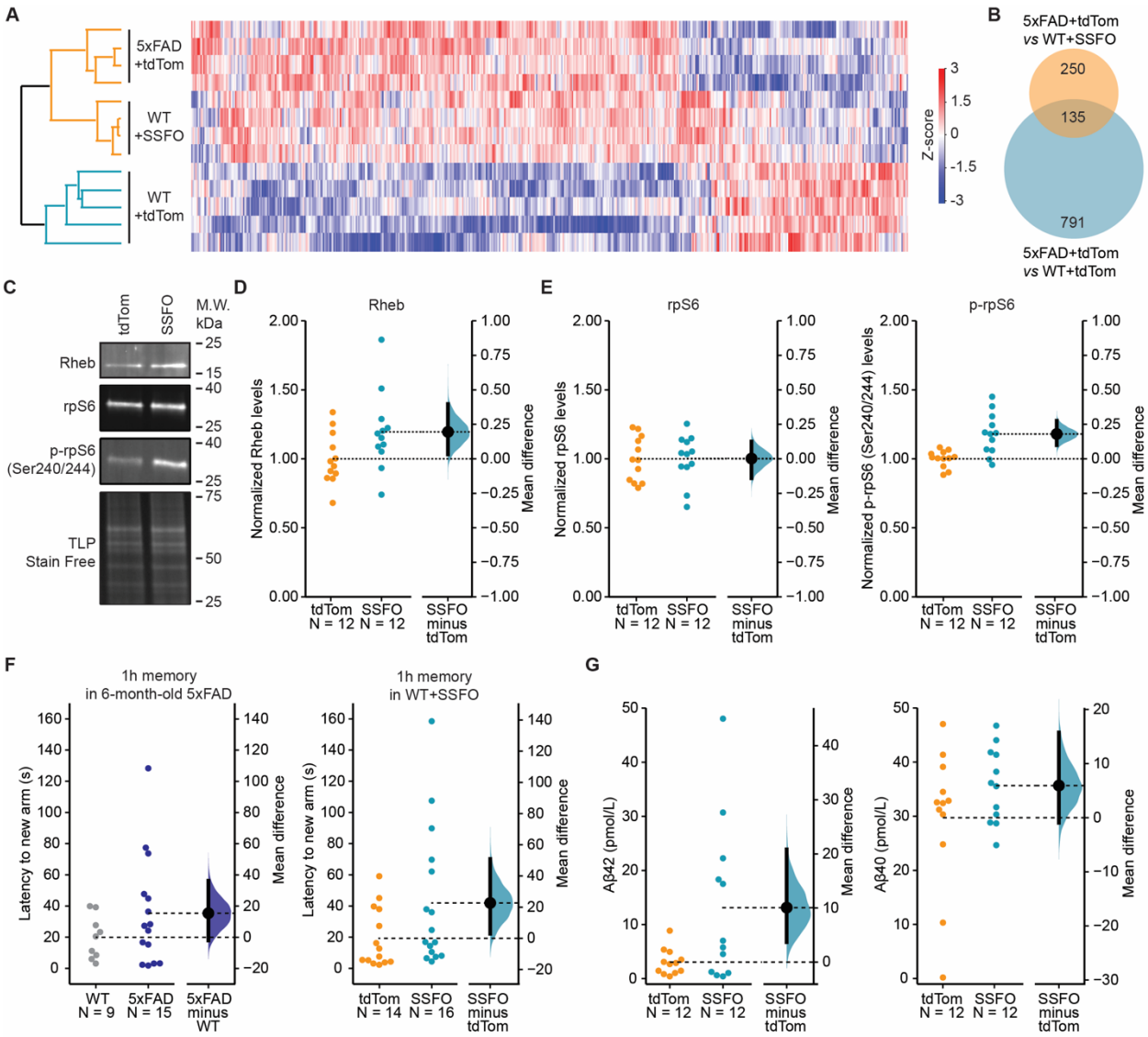

Fig. 6: Chronic hippocampal optogenetic activation induces spatial memory deficits and augments Aβ42 secretion in wild-type mice. (**A**) Heat map revealing the hierarchical clustering of 5xFAD and WT mice expressing SSFO or tdTomato based on their scaled protein levels in the hippocampus after 4 weeks of daily optogenetic stimulation. (**B**) Venn diagram showing the number of common proteins when comparing the altered proteins in 5xFAD mice as compared to WT (5xFAD+tdTom *vs* WT+tdTom) and the proteins altered between the 5xFAD+tdTom and the WT+SSFO. (**C**) Representative immunoblots of hippocampal lysates from WT+SSFO and WT+tdTom mice. (**D**) The protein levels of Rheb in WT+SSFO and WT+tdTom mice. (**E**) Quantification of ribosomal protein S6 (rpS6) expression (left) and its phosphorylation levels at the Ser240/204 residues. (**F**) The latency to the new arm during the one hour Y-maze spatial memory test for 6-month-old 5xFAD mice (n = 15) and their non-transgenic littermates (WT; n =

663 9). (**G**) The latency to the new arm during the one hour Y-maze spatial memory test for WT+SSFO
664 mice (*n* =12) *vs* WT+tdTom mice (*n* = 12). (**H**) The concentration of soluble Aβ40 and Aβ42 in the
665 hippocampus of WT+SSFO mice as compared to WT+tdTom. The data are analyzed with
666 estimation statistics. Each point represents an individual mouse. The mean difference is
667 dissipated as a dot and the 95% confidence interval by the ends of the vertical error bars.
668

669 **Supplementary Figures**

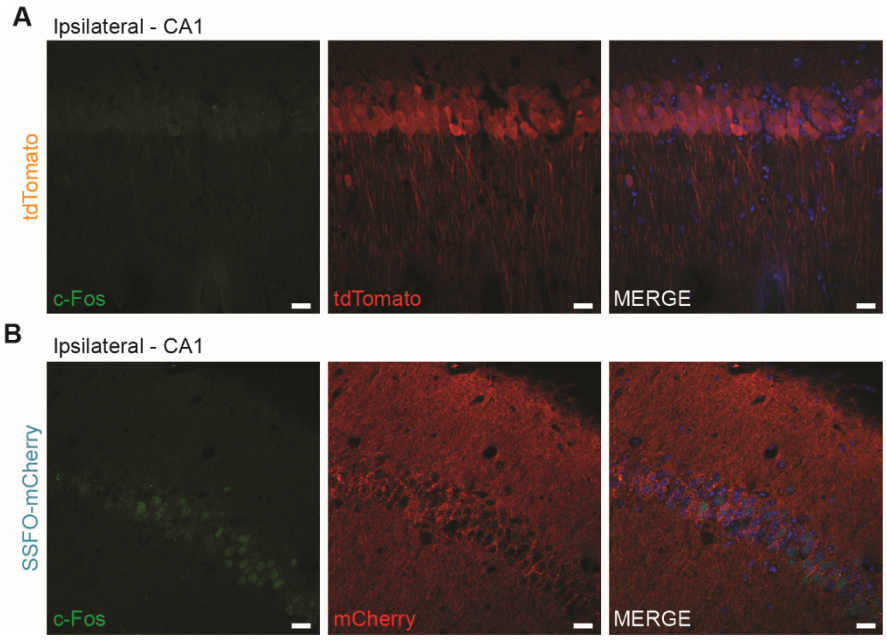

670
671 **Supplementary Fig. S1: c-Fos expression in the hippocampus of AAV-CaMKIIa-tdTomato**
672 **or AAV-CaMKIIa-SSFO-mCherry infected mice.** (**A**) Confocal images showing labeling for c-
673 Fos (green) and tdTomato (reporter protein, red) in coronal sections of mice infected with AAV-
674 CaMKIIa-tdTomato. (**B**) Confocal images showing labeling for c-Fos (green) and Cherry (SSFO
675 expression reporter protein, red) in coronal sections of mice infected with AAV-CaMKIIa-SFFO.
676 Scale bars 20 μm, DAPI in blue.

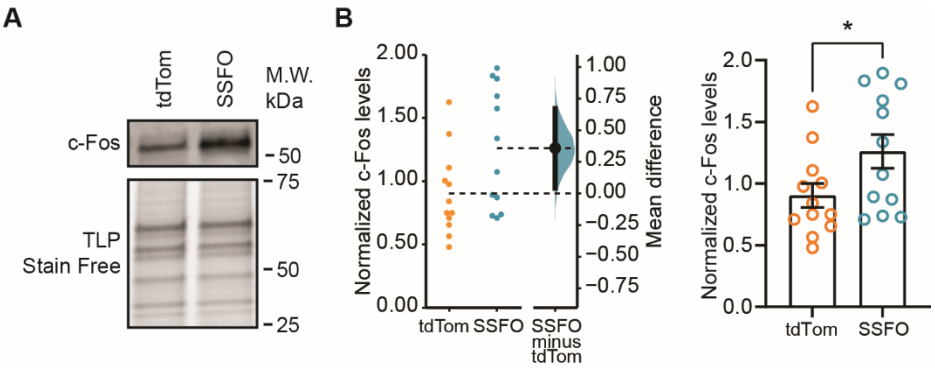

Supplementary Fig. S2: c-Fos is upregulated in the hippocampus of SSFO expressing wildtype mice. (**A**) Representative immunoblots for the levels of c-Fos in hippocampal samples from WT+tdTom and WT+SSFO mice. (**B**) Quantification of c-Fos protein levels measured by immunoblotting in WT+SSFO (cyan; *n* = 12) and WT+tdTom (orange; *n* = 12) mice. Data are represented as the mean difference (dot) and the 95% confidence interval (by the ends of the error bars; left) or as mean ± SEM (right). *P < 0.05.

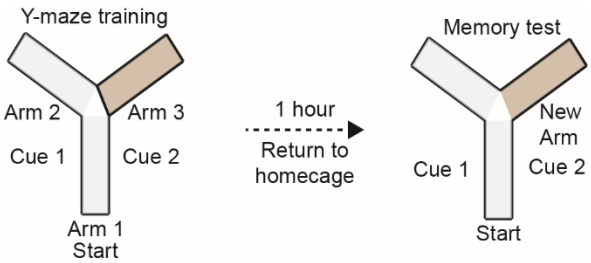

Supplementary Fig. S3: Y-maze spatial memory test. Schematic representation of the modified version of the Y-maze alternation test for assessing short-term spatial memory performance in rodents.

688 ## Supplementary Tables

689 **Supplementary Table S1: The differentially expressed proteins upon chronic optogenetic**
690 **stimulation of the hippocampus in wildtype mice.** Proteins are identified by their gene name
691 together with their UniProt ID number. Average log2 fold differences and P-values have been
692 calculated as described in Methods. The log2 fold change becomes positive when WT+SSFO >
693 WT+tdTom and negative when WT+SSFO < WT+tdTom. P-value determines the statistical
694 significance (*P < 0.05).
695
696 **Supplementary Table S2: Differentially regulated proteins in the hippocampus of 3-month-**
697 **old 5xFAD.** Gene name and UniProt ID number are used to identify proteins. The log2 fold
698 change becomes positive when 5xFAD+tdTom > WT+tdTom and negative when 5xFAD+tdTom
699 < WT+tdTom. P-value determines the statistical significance (*P < 0.05).
700
701 **Supplementary Table S3: The proteins altered in levels in the hippocampus of 5xFAD mice**
702 **upon chronic optogenetic stimulation.** Proteins are identified by their gene name and their
703 UniProt ID number is provided. The log2 fold change becomes positive when 5xFAD+SSFO >
704 5xFAD+tdTom and negative when 5xFAD+SSFO < 5xFAD+tdTom. P-value determines the
705 statistical significance (*P < 0.05).

Supplementary Data

Original, uncropped immunoblots and TGX Stain Free gels related to Figure 2

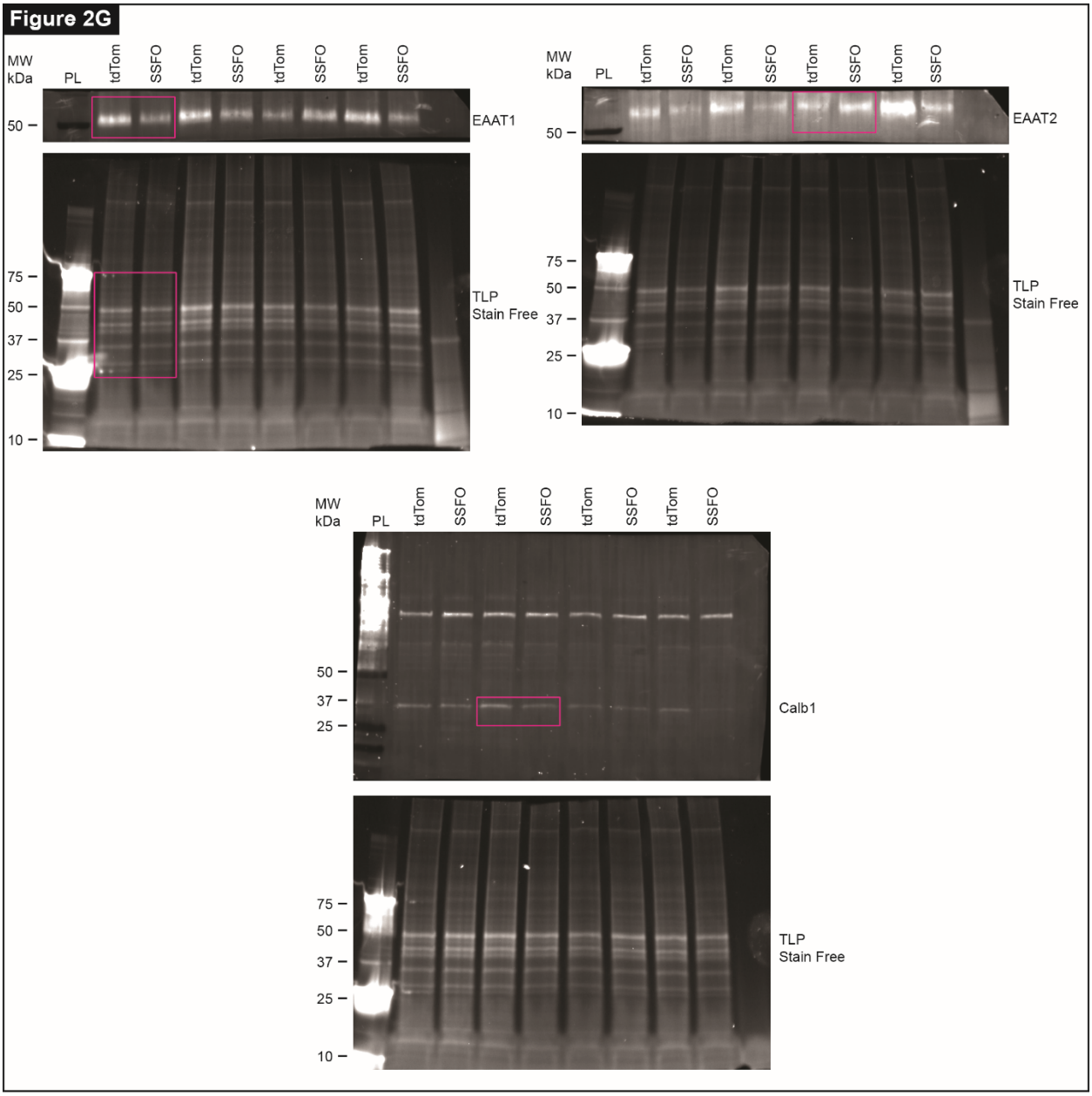

Original, uncropped immunoblots and TGX Stain-Free gels related to Figure 6

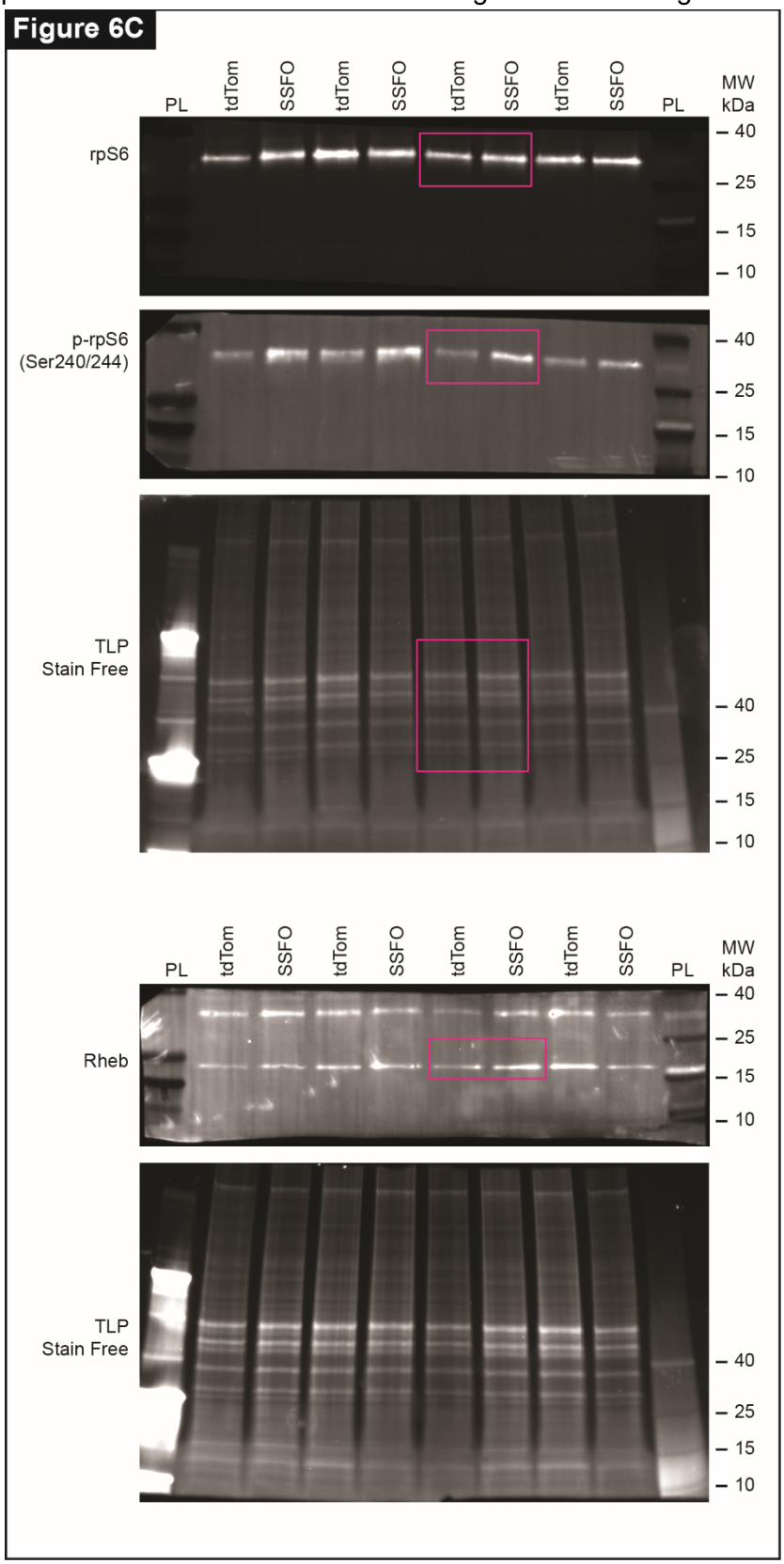
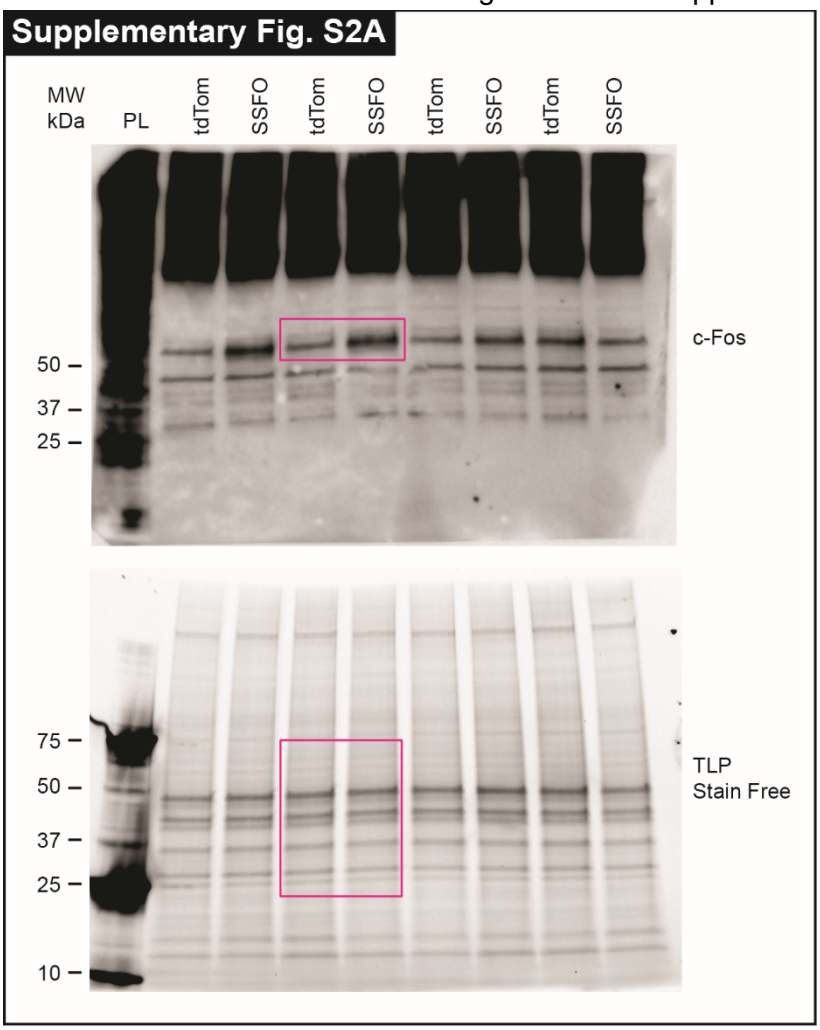
Original, uncropped immunoblot and TGX Stain Free gel related to Supplementary Fig. S3